THE JOURNAL OF PHYSICAL CHEMISTRY C

Article

pubs.acs.org/JPCC

Effect of Doping Metals on OMS-2/γ-Al_2O_3 Catalysts for Plasma-Catalytic Removal of *o*-Xylene

Lian Wang,[†] Changbin Zhang,[*,†] Hong He,[†] Fudong Liu,[†] and Caixia Wang[†,‡]

[†]State Key Joint Laboratory of Environment Simulation and Pollution Control, Research Center for Eco-Environmental Sciences, Chinese Academy of Sciences, Beijing 100085, China

[‡]State Key Laboratory of Chemical Resource Engineering, Beijing University of Chemical Technology, Beijing 100029, China

ABSTRACT: A series of Pd-, Ce-, Co-, and Ti- doped OMS-2 catalysts were prepared by a one-step hydrothermal method. The removal of *o*-xylene by a combination of metal-doped OMS-2/γ-Al_2O_3 catalysts and nonthermal plasma was systematically investigated. Catalysts were characterized by inductively coupled plasma optical emission spectrometry (ICP-OES), X-ray diffraction (XRD), field emission scanning electron microscopy (FE-SEM), extended X-ray absorption fine structure (EXAFS), X-ray photoelectron spectroscopy (XPS), and H_2 temperature-programmed reduction (H_2-TPR). Among the metal-doped OMS-2/γ-Al_2O_3 catalysts used in the plasma-catalytic process, $Pd_{0.07}$-OMS-2/γ-Al_2O_3 and $Ce_{0.07}$-OMS-2/γ-Al_2O_3 exhibited excellent catalytic activity for *o*-xylene removal with 100% *o*-xylene conversion, above 60% CO_2 selectivity, and above 80% ($CO+CO_2$) (i.e., CO_x) yield at a low specific energy density of 18 J/L. These two catalysts had high redox ability, abundant surface defects for absorbing and activating oxygen, and more active surface oxygen species than $Co_{0.07}$-OMS-2/γ-Al_2O_3 and $Ti_{0.07}$-OMS-2/γ-Al_2O_3 catalysts, therefore resulting in much higher catalytic activity in the oxidation of *o*-xylene. The concentration of byproducts produced by nonthermal plasma such as O_3 and NO_x was greatly reduced when using these metal-doped OMS-2/γ-Al_2O_3 catalysts. $Pd_{0.07}$-OMS-2/γ-Al_2O_3 had the highest suppression ability for O_3 and NO_x, which were reduced to near zero. Moreover, Fourier transform infrared spectroscopy (FT-IR) results suggested that introduction of metal-doped OMS-2/γ-Al_2O_3 catalysts could oxidize *o*-xylene to CH_3CHO and/or CH_3COOH and further oxidize CH_3CHO and/or CH_3COOH to CO or CO_2.

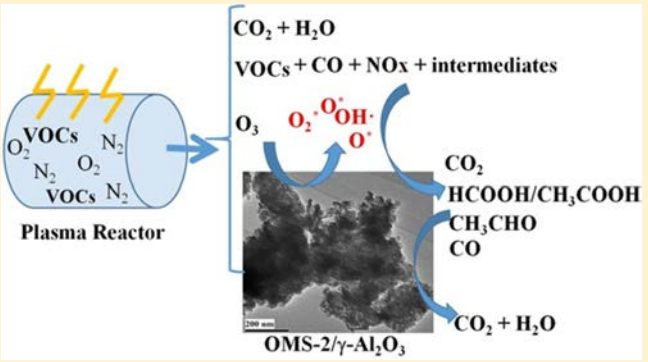

1. INTRODUCTION

As typical hazardous air pollutants, benzene, toluene, and xylene (BTX) have the potential to be highly toxic to the environment and human health. Removal of BTX for air purification is of great significance and has attracted great attention.[1,2] In recent years, nonthermal plasma (NTP) technology has aroused growing interest from scientists due to its high efficiency in removal of BTX at low temperatures through generation of strong oxidizing agents like ozone, hydroxyl radical, atomic oxygen, etc.[3−5] However, the NTP technique has some disadvantages such as formation of large amounts of toxic byproducts and low CO_2 selectivity for volatile organic compounds (VOCs) abatement, because energy of radicals formed in the discharge process is not high enough for complete oxidation of BTX.[5] Therefore, one of the most efficient strategies is the combination of NTP and catalysis to overcome the drawbacks of NTP for the removal of BTX.[5−18] Catalysts could further oxidize the byproducts formed in the plasma process to reduce the production of byproducts and raise CO_2 selectivity.

In order to efficiently remove BTX through combining NTP and catalysis, one of the key requirements is to find an excellent catalyst with high catalytic performance. Reactive oxygen species such as atomic oxide species and superoxide radicals generated from decomposition of ozone play important roles in the oxidation of VOCs in plasma-catalytic process.[17,18] Therefore, catalysts that can efficiently decompose ozone are promising candidates to be used in plasma-catalytic processes. Among transition metal oxide, manganese oxide (MnO_x) is the most active metal oxide for decomposition of ozone.[19] As reported, MnO_x based catalysts have shown high catalytic activity for removal of BTX in the plasma-catalytic process.[10−12]

Octahedral molecular sieve of manganese oxide (OMS-2) is a form of manganese dioxide with a one-dimensional tunnel structure composed of 2 × 2 MnO_6 octahedral chains. OMS-2 has many attractive advantages such as large surface area, abundant pores and tunnel structure, and ion-exchange ability when used as a catalyst. Wang et al. have reported on the high ozone decomposition activity of OMS-2.[20] Thus, OMS-2 has high potential as a catalyst to be used in plasma-catalytic process for VOCs removal. As a matter of fact, OMS-2 has been extensively exploited for the total oxidation of VOCs with

Received: January 26, 2016
Revised: March 2, 2016
Published: March 7, 2016

DOI: 10.1021/acs.jpcc.6b00870
J. Phys. Chem. C 2016, 120, 6136−6144

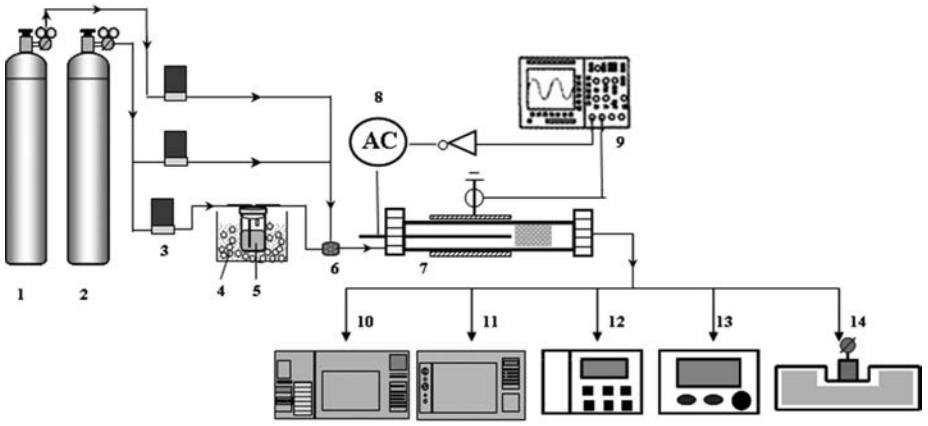

Figure 1. Schematic diagram of the experimental setup. 1. Oxygen, 2. nitrogen, 3. mass flow controller, 4. ice bath, 5. gas bubbler, 6. gas mixer, 7. plasma reactor, 8. AC high voltage supply, 9. oscilloscope, 10. GC-MS, 11.GC, 12. NO_x analyzer, 13. O_3 analyzer, and 14. FT-IR.

superior catalytic activity.[21−26] Furthermore, the properties of OMS-2, such as the surface area and redox ability, can be optimized through replacing tunnel K^+ ions or framework Mn ions by various metal ions, such as Cu^{2+}, Zn^{2+}, Ni^{2+}, Co^{2+}, Fe^{3+}, Mg^{2+}, etc., to enhance their catalytic performance.[27,28] The incorporation of different ions into the tunnel or in the framework of OMS-2 materials might promote the generation of defects to enhance oxygen mobility. Shangguan et al. recently reported high removal efficiency for VOCs by combining plasma and a Co-OMS-2 catalyst.[29] However, according to our knowledge, study on the use of metal-doped OMS-2 for BTX removal combined with nonthermal plasma has rarely been reported.

Among noble metal catalysts, Pd-based catalysts have been extensively studied due to their high catalytic activity for catalytic oxidation of BTX.[30] In rare earth materials, Ce-based catalysts were found to be very active toward VOCs oxidation because of their high oxygen storage capacity and oxygen mobility.[2] Among transition metal catalysts, Co-based catalysts exhibit excellent catalytic activity for VOCs oxidation.[31,32] NTP in air can produce ultraviolet radiation due to excited nitrogen molecules, thus the addition of Ti could possibly improve VOCs removal efficiency.[33] Therefore, in this study, Pd^{2+}, Ce^{3+}, Co^{2+}, and Ti^{4+} -doped OMS-2 catalysts were prepared and tested for catalytic conversion of *o*-xylene by adding catalysts downstream from the discharge zone of a dielectric barrier discharge (DBD) plasma. Catalysts were characterized by ICP-OES, XRD, BET, FE-SEM, XPS, H_2-TPR, and EXAFS methods. Effects of different dopants on chemical properties such as Mn valence, crystal phases, surface oxygen contents, oxygen defects, and oxidation−reduction properties were investigated and subsequently correlated with catalytic activity.

2. EXPERIMENTAL SECTION

2.1. Experimental Setup and Methods. Figure 1 shows a schematic diagram of the experimental setup, which consists of three parts, a cylindrical plasma reactor with an inner high-voltage electrode, reaction gas supply, and analytical instruments. The discharge reactor had a coaxial geometry (inner diameter 8 mm, outer diameter 18 mm, and length 400 mm) with a quartz tube as dielectric between the inner high-voltage electrode (aluminum, diameter 8 mm and length 100 mm) and a grounded electrode (aluminum foil, diameter 18 mm and length 100 mm) on the outer quartz tube wall to form a 100 mm length DBD zone. The gas discharges were produced by a high-frequency AC high-voltage power supply source. In addition, catalysts (1.5 g, 40−60 mesh) were placed after the discharge zone. The reactant feed was composed of 9 ppm *o*-xylene, 20 vol % O_2 and 80 vol % N_2 (total flow rate = 6 L min^{-1}), mixed in a mixing chamber before the reactor. The discharge was started when the concentration of *o*-xylene at the outlet reached a steady state. All experiments were repeated in triplicate. The experimental results were obtained from the average values of three experiments.

Discharge power was measured by the V-Q Lissajous program. The charge Q was measured from the voltage across a capacitor of 100 nF connected in series to the ground electrode. The applied voltage was measured with a 1000:1 high-voltage probe (Tektronix TPP0201). The waveforms of the charge Q and the applied voltage were monitored using a digital oscilloscope (Tektronix TDS 2012c) and plotted to obtain the Lissajous diagram.

The *o*-xylene conversion, CO_2 selectivity, CO_x yield, and specific energy density in the gas phase were defined as follows:

$$o\text{-xylene conversion}(\%) = [o\text{-xylene}]_{outlet}/[o\text{-xylene}]_{inlet} \times 100$$

$$\text{carbon dioxide selectivity}(\%) = [CO_2]/8[C_8H_{10}]_{conversion} \times 100$$

Carbon dioxide and carbon monoxide yield:

$$CO_x\text{yield}(\%) = ([CO] + [CO_2])/8[C_8H_{10}]_{conversion} \times 100$$

$$\text{specific energy density: SED(J/L)} = \text{discharge power(W)}/\text{gas flow rate(L/min)} \times 60$$

The *o*-xylene concentration was analyzed online by a gas chromatograph (GC; Agilent 6890, HP 5MS). CO_2 and CO concentrations were analyzed by a GC equipped with flame ionization detector (Shangfen GC-112A, TDX-01 column). O_3 and NO_x concentrations were determined by an O_3 detector (model 202, 2B Technology) and NO_x detector (Thermal 42i). Other oxidation products were detected by online FT-IR (Thermo Scientific Nicolet is50).

2.2. Catalyst Preparation. The OMS-2 was prepared with a hydrothermal method according to the procedure used by

DOI: 10.1021/acs.jpcc.6b00870
J. Phys. Chem. C 2016, 120, 6136−6144

Luo et al.[34] 3.668 g of $MnAc_2{\cdot}4H_2O$ was dissolved in deionized water, and 2.5 mL of glacial acetic acid was then added. Next a solution containing 2.168 g of $KMnO_4$ was added to the above mixture. Finally the mixed solution was placed in a Teflon-lined autoclave maintained at 100 °C for 24 h and then cooled to room temperature. The resulting black slurry was centrifuged, washed, and dried at 100 °C before calcined at 400 °C for 4 h in air.

A series of metal-doped OMS-2 catalysts was prepared via a one-step hydrothermal synthesis. For example, the detailed procedure of Pd-OMS-2 preparation was as follows: 3.668 g of $MnAc_2{\cdot}4H_2O$ and 0.402 g of $Pd(NO_3)_2{\cdot}2H_2O$ were dissolved in deionized water, and then 2.5 mL of glacial acetic acid was added. Next solution containing 2.168 g $KMnO_4$ was added to the above mixture. Finally the mixed solution was maintained at 100 °C for 24 h in a Teflon-lined autoclave. The resulting black slurry was centrifuged, washed with deionized water and dried at 100 °C overnight and then calcined at 400 °C for 4 h in air. The synthesis of Ce-, Co-, and Ti-OMS-2 followed the above procedure at the required mole ratio. Metal-doped OMS-2/γ-Al_2O_3 catalysts were prepared by mixing metal-doped OMS-2 samples with γ-Al_2O_3 powder through ball-milling.

For comparison, Pd, Ce, Co, and Ti/γ-Al_2O_3 catalysts loaded with equal metal amounts were prepared with an impregnation method. The obtained powders were dried at 100 °C overnight and calcined at 400 °C for 4 h in air. An ion-exchange method was also used for Ce-OMS-2 preparation. K^+ in the tunnel of OMS-2 was first exchanged by adding OMS-2 into 1 mol L^{-1} NH_4NO_3 solution and stirred at 70 °C for 6 h. Next the mixture was filtered, washed, and dried at 100 °C overnight and then calcined at 400 °C for 6 h in air. Thus, H-OMS-2 was formed.[35] H^+ in the tunnel was then exchanged by Ce^{3+} following the same procedure.

The amounts of Mn element and doped metals of prepared catalysts were examined by ICP-OES measurements. Catalysts were dissolved with concentrated HNO_3 and concentrated HCl with a volume ratio of 1:3. Then, the solution was diluted to 50 mL, followed by ICP-OES measurement on an Optima 2000 (Perkin–Elmer Co.). The content of Mn was around 6 wt % for all catalysts, as determined by ICP-OES. The molar ratio of doped metal with Mn element was also confirmed by ICP-OES. Catalysts containing the low molar ratio of 0.07 of doped metals to Mn were used in this work based on considering OMS-2 as KMn_8O_{16}.

2.3. Catalyst Characterization. The XRD patterns of catalysts were recorded on an X-ray diffractometer (PANalytical X'Pert PRO, Japan) with Cu Kα radiation (λ = 0.154 nm). Nitrogen adsorption–desorption isotherms were measured using a Quantachrome Autosorb-1C instrument at 77 K. The surface area of the catalysts was calculated by the Brunauer–Emmett–Teller (BET) method. The volume of pores was determined by the Barrett–Joyner–Halenda (BJH) method from the desorption branches of the isotherms. FE-SEM measurements were performed on a SU-8000 electron microscope (Hitachi, Japan). XPS measurements were carried out on a Thermo ESCALAB 250 spectrometer (Vacuum Generators, USA) using Al Kα radiation. The spectra were corrected by referencing the C 1s peak at 284.8 eV. H_2-TPR was also performed on a Chemisorption Analyzer (AutoChem 2920). Prior to the TPR experiments, the samples (100 mg) were pretreated at 400 °C in a flow of 20 vol % O_2/Ar (50 mL/min) for 1 h and cooled to room temperature. Then the samples were exposed to a flow of 10 vol % H_2/Ar (30 mL/min) at 30 °C for 1 h, followed by raising the temperature to 600 °C at a rate of 10 °C/min. The XANES and EXAFS of the Mn–K edge in metal-doped OMS-2 catalysts and Mn-containing reference samples were measured in a transmission mode at room temperature on the BL14W1 beamline, Shanghai Synchrotron Radiation Facility (SSRF). The storage ring was operated at 3.5 GeV with 200 mA as an average storage current. The synchrotron radiation was monochromatized with a Si (111) double crystal monochromator. XAFS data were analyzed using the REX2000 program (RigakuCo.). The EXAFS oscillation function $\chi(k)$ was extracted using spline smoothing with a Cook-Sayers criterion,[36] and the filtered k^3-weighted $\chi(k)$ was Fourier transformed into R space in the k range of 2.5–13 $Å^{-1}$. In the curve-fitting step, the possible back scattering amplitude and phase shift were calculated using FEFF8.4 code.[37]

3. RESULTS AND DISCUSSION

3.1. *o*-Xylene Removal Efficiency. The catalytic performance of OMS-2/γ-Al_2O_3 and metal-doped OMS-2/γ-Al_2O_3 catalysts in the plasma-catalytic system were first examined. Figure 2 presents the *o*-xylene conversion, CO_2 selectivity and CO_x yield at various specific energy densities (SED). When plasma alone used, *o*-xylene conversion, CO_2 selectivity, and CO_x yield were 60%, 49%, and 60% at SED of 18 J/L, respectively. It is clear that the introduction of catalysts significantly improved the *o*-xylene removal efficiency, CO_2 selectivity, and CO_x yield compared to the case of plasma alone. Comparing the catalytic activity of OMS-2/γ-Al_2O_3 before and after doping with metals, the metal-doped samples all showed much higher activity than the undoped sample. In addition, pure Pd, Ce, Co, and Ti supported on γ-Al_2O_3 catalysts with equal metal amounts were also prepared and tested. The results (Figure 2) showed that the Pd, Ce, Co, and Ti/γ-Al_2O_3 were less effective than the corresponding metal-doped OMS-2/γ-Al_2O_3 catalysts, respectively. Therefore, there was a synergistic effect between the doping metal and OMS-2, which greatly improved the catalytic activity. In particular, the addition of $Pd_{0.07}$-OMS-2/γ-Al_2O_3 and $Ce_{0.07}$-OMS-2/γ-Al_2O_3 yielded high catalytic activity with 100% o-xylene conversion, high CO_2 selectivity and CO_x yield, even at a low SED of 18 J/L.

3.2. Catalyst Characterization. The catalytic activities of metal-doped OMS-2/γ-Al_2O_3 catalysts were closely related to their physical and chemical properties. Therefore, these catalysts were next characterized by several methods. XRD was first used to determine the effects of metals dopants on the OMS-2 crystalline structure and the crystalline state of the doped metals. Figure 3 shows the XRD patterns of a series of OMS-2/γ-Al_2O_3 catalysts with 0.07 molar ratio of doped metal to Mn. Diffraction peaks appearing at 2θ = 12.6°, 17.9°, 28.7°, 37.5°, 41.9°, 49.9°, and 60.1° could be attributed to the typical crystalline phase of cryptomelane (KMn_8O_{16}, JCPDS 29-1020). No other crystalline peaks appeared, indicating that metal ions may either be incorporated into cryptomelane structure or exist in a high dispersed state. Compared with the pattern of OMS-2 in OMS-2/γ-Al_2O_3, the diffraction peaks of the (411) and (521) crystal planes of OMS-2 in the $Pd_{0.07}$-OMS-2/γ-Al_2O_3, $Co_{0.07}$-OMS-2/γ-Al_2O_3, and $Ti_{0.07}$-OMS-2/γ-Al_2O_3 samples had a slight shift toward higher angle. The largest shift of 0.6° was observed for the diffraction peak of the (411) crystal plane in $Co_{0.07}$-OMS-2/γ-Al_2O_3. The shift of XRD patterns after doping suggested the existence of tensile strain and lattice change, which implied that the doped metal ions partially replaced Mn

DOI: 10.1021/acs.jpcc.6b00870
J. Phys. Chem. C 2016, 120, 6136–6144

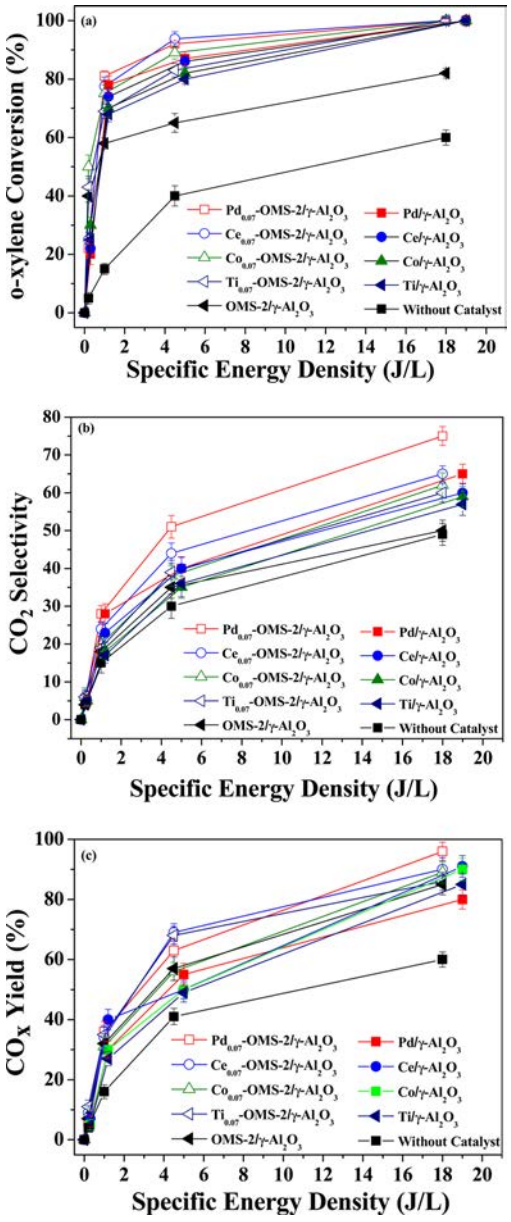

Figure 2. (a) *o*-Xylene conversion, (b) CO_2 selectivity, and (c) CO_x yield using metal-doped OMS-2/γ-Al_2O_3 catalysts.

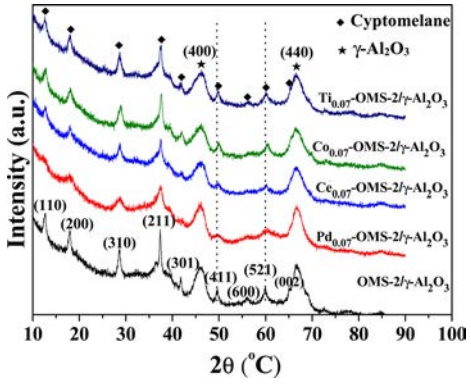

Figure 3. XRD patterns of metal-doped OMS-2/γ-Al_2O_3 catalysts.

ions in $Pd_{0.07}$-OMS-2/γ-Al_2O_3, $Co_{0.07}$-OMS-2/γ-Al_2O_3, and $Ti_{0.07}$-OMS-2/γ-Al_2O_3 catalysts, due to the change of ionic radii.[38,39] Moreover, the low crystallinity of $Pd_{0.07}$-OMS-2/γ-Al_2O_3 and $Ce_{0.07}$-OMS-2/γ-Al_2O_3 implied the presence of abundant defects induced by reachieving charge balance when Pd and Ce were doped into the tunnel or in the framework of OMS-2 materials and replaced K or Mn ions.[40] In addition, the high oxygen storage capacity and oxygen mobility of Ce and high oxidation ability of Pd might be also conducive to the formation of defects.[2]

The morphology of catalysts was observed by FE-SEM measurements. A porous structure with some pseudoflakes appeared for OMS-2/γ-Al_2O_3 (Figure 4). After doping with Pd

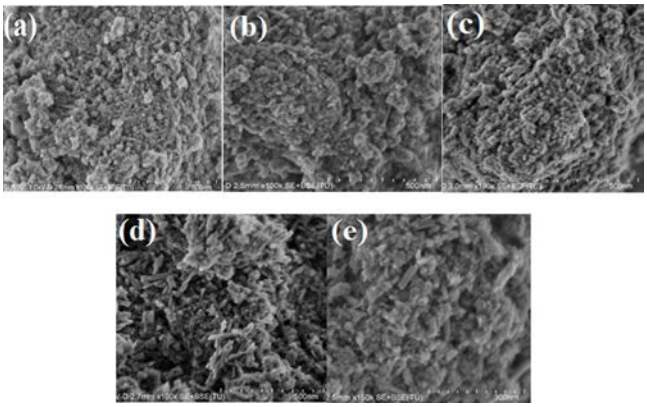

Figure 4. FE-SEM micrographs of OMS-2/γ-Al_2O_3 catalysts. (a) OMS-2/γ-Al_2O_3, (b) $Pd_{0.07}$-OMS-2/γ-Al_2O_3, (c) $Ce_{0.07}$-OMS-2/γ-Al_2O_3, (d) $Co_{0.07}$-OMS-2/γ-Al_2O_3, and (e) $Ti_{0.07}$-OMS-2/γ-Al_2O_3.

and Ce, little change was found, while a number of rods appeared for $Co_{0.07}$-OMS-2/γ-Al_2O_3 and $Ti_{0.07}$-OMS-2/γ-Al_2O_3 and the particle size increased, which was larger than those of $Pd_{0.07}$-OMS-2/γ-Al_2O_3 and $Ce_{0.07}$-OMS-2/γ-Al_2O_3.

To examine the structural and valence information on catalysts, the XAFS of the Mn−K edge, including XANES and EXAFS, was measured using Mn foil, MnO, Mn_2O_3, and MnO_2 as reference samples. As shown in Figure 5a, both the pre-edge peaks and the postedge regions of Mn−K XANES in OMS-2/γ-Al_2O_3 before and after doping with metals were similar to those in MnO_2. Thus, no significant differences in Mn valences were observed among the catalysts doped with different metals. To further determine the average valence of Mn species in

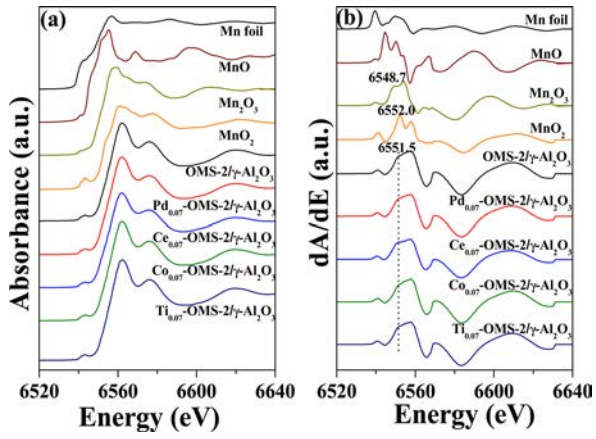

Figure 5. (a) XANES and (b) first-order derivatives of XANES of Mn−K edge in series of catalysts and Mn-containing reference samples.

DOI: 10.1021/acs.jpcc.6b00870
J. Phys. Chem. C 2016, 120, 6136−6144

catalysts, the first-order derivatives of Mn−K XANES in OMS-2/γ-Al_2O_3 catalysts were taken and compared with those in the reference samples (Figure 5b). The Mn K-edge absorption energies of the reference samples were 6548.7 and 6552.0 eV for Mn_2O_3 and MnO_2, respectively. The absorption edge energy of Mn species in all doped and undoped OMS-2/γ-Al_2O_3 catalysts was 6551.5 eV, which was slightly less than that in MnO_2, most probably due to the presence of a small amount of Mn^{3+}. These results and XRD results indicated that the crystal structure of MnO_x over all these OMS-2/γ-Al_2O_3 catalysts was mainly the α-MnO_2 crystal phase (JCPDS 44-0141).

An EXAFS experiment was used to explore the minor changes in the catalyst structure, such as coordination number and bond distance. Figure 6a shows the Fourier transformed

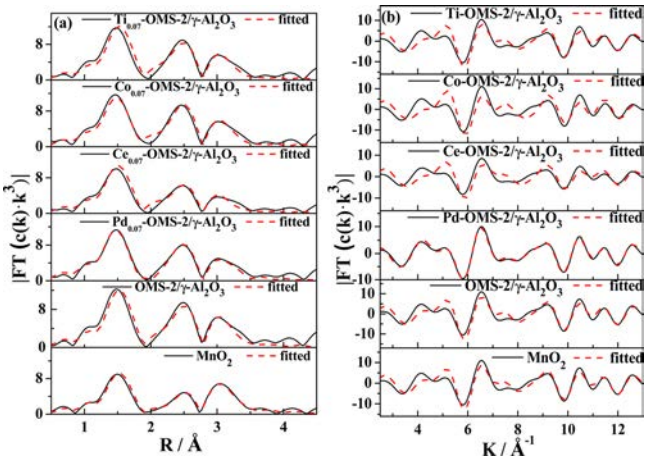

Figure 6. EXAFS spectra of Mn K-edge in metal-doped OMS-2/γ-Al_2O_3 catalysts. (a) Fourier transforms of filtered $k^3\cdot\chi(k)$ into R space and (b) filtered $k^3\cdot\chi(k)$ in the k range of 2.5−13 Å^{-1}.

filtered k^3-weighted EXAFS oscillations Fourier transformed into R space for the Mn−K edge in OMS-2/γ-Al_2O_3 catalysts, and Figure 6 (b) shows the corresponding filtered $k^3\cdot\chi(k)$ in the k range of 2.5−13 Å^{-1}. Although the crystal structure of our metal-doped OMS-2/γ-Al_2O_3 catalysts was α-MnO_2, the coordination peaks in the second shell, i.e., the relative peak intensity of Mn−Mn_1 and Mn−Mn_2, are different compared with those in the MnO_2 standard sample. The curve-fitted data are presented in Table 1. It was obvious that the second coordination shells of Mn−Mn_1 and Mn−Mn_2 in the series of OMS-2/γ-Al_2O_3 catalysts were not the same as in MnO_2. $Pd_{0.07}$-OMS-2/γ-Al_2O_3 and $Ce_{0.07}$-OMS-2/γ-Al_2O_3 show a relatively small coordination number of Mn−Mn_1 and Mn−Mn_2 coordination shell. These results indicated that more surface defects might exist on $Pd_{0.07}$-OMS-2/γ-Al_2O_3 and $Ce_{0.07}$-OMS-2/γ-Al_2O_3; therefore, these two samples should have high oxygen storage capacity and oxygen mobility, which is beneficial for *o*-xylene oxidation.[41]

The XPS experiment was performed to verify the state and atomic concentration of Mn on the catalyst surface. XPS results are shown in Figure 7 and listed in Table 2. Mixed valency manganese ions were observed, including Mn^{4+} and Mn^{3+}.[42,43] Mn^{3+} was the main valence on the catalyst surface, which was opposite to that in the bulk phase of the catalysts. $Pd_{0.07}$-OMS-2/γ-Al_2O_3 had the highest ratio of surface oxygen or defective oxygen (O_{sur}) to lattice oxygen (O_{latt}), and $Ce_{0.07}$-OMS-2/γ-Al_2O_3 had the second highest ratio. Obviously, $Pd_{0.07}$-OMS-2/γ-Al_2O_3 and $Ce_{0.07}$-OMS-2/γ-Al_2O_3 were richer in O_{sur} species on the surface, which generally play an important role in catalytic oxidation reactions. Formation of abundant active oxygen for $Pd_{0.07}$-OMS-2/γ-Al_2O_3 and $Ce_{0.07}$-OMS-2/γ-Al_2O_3 was due to their small particle size (Figure 3) and higher number of surface defects that could activate oxygen to surface active oxygen species, resulting in much higher catalytic activity toward complete oxidation of *o*-xylene.

To examine the redox ability, H_2-TPR experiments were performed. Figure 8 shows the H_2-TPR profiles of OMS-2/γ-Al_2O_3 catalysts. Two peaks of H_2 consumption were observed at 290 and 360 °C, and the ratio of the low-temperature peak to the high-temperature peak was about 2 for OMS-2/γ-Al_2O_3. The low-temperature peak should be attributed to reduction of MnO_2 to Mn_3O_4, while the high-temperature peak should be

Table 1. Curve-Fitting Results of Mn K-Edge EXAFS in Metal-Doped OMS-2/γ-Al_2O_3 Catalysts

catalysts	Mn−K reference	shell	CN[a]	e.s.d.[b]	R[c] (Å)	DW[d]	R factor (%)
MnO_2	α-MnO_2	Mn−O	6.0	0.14	1.90	0.07	0.5
		Mn−Mn_1	3.9	0.20	2.85	0.09	
		Mn−Mn_2	4.1	0.12	3.44	0.05	
OMS-2/γ-Al_2O_3	α-MnO_2	Mn−O	6.6	0.12	1.91	0.06	5.4
		Mn−Mn_1	**5.0**	0.16	2.88	0.08	
		Mn−Mn_2	**3.4**	0.14	3.45	0.05	
$Pd_{0.07}$-OMS-2/γ-Al_2O_3	α-MnO_2	Mn−O	6.5	0.19	1.90	0.06	1.5
		Mn−Mn_1	**4.5**	0.19	2.89	0.08	
		Mn−Mn_2	**3.1**	0.20	3.46	0.05	
$Ce_{0.07}$-OMS-2/γ-Al_2O_3	α-MnO_2	Mn−O	6.7	0.08	1.92	0.06	5.2
		Mn−Mn_1	**3.9**	0.12	2.88	0.07	
		Mn−Mn_2	**2.1**	0.07	3.45	0.04	
$Co_{0.07}$-OMS-2/γ-Al_2O_3	α-MnO_2	Mn−O	6.8	0.13	1.90	0.07	4.9
		Mn−Mn_1	**4.9**	0.14	2.88	0.06	
		Mn−Mn_2	**3.5**	0.13	3.45	0.05	
$Ti_{0.07}$-OMS-2/γ-Al_2O_3	α-MnO_2	Mn−O	6.8	0.12	1.90	0.06	6.1
		Mn−Mn_1	**4.9**	0.15	2.88	0.08	
		Mn−Mn_2	**3.4**	0.13	3.45	0.05	

[a]CN: coordination number. [b]e.s.d: estimated standard deviation of coordination number. [c]R: bond distance. [d]DW: Debye−Waller factor.

DOI: 10.1021/acs.jpcc.6b00870
J. Phys. Chem. C 2016, 120, 6136−6144

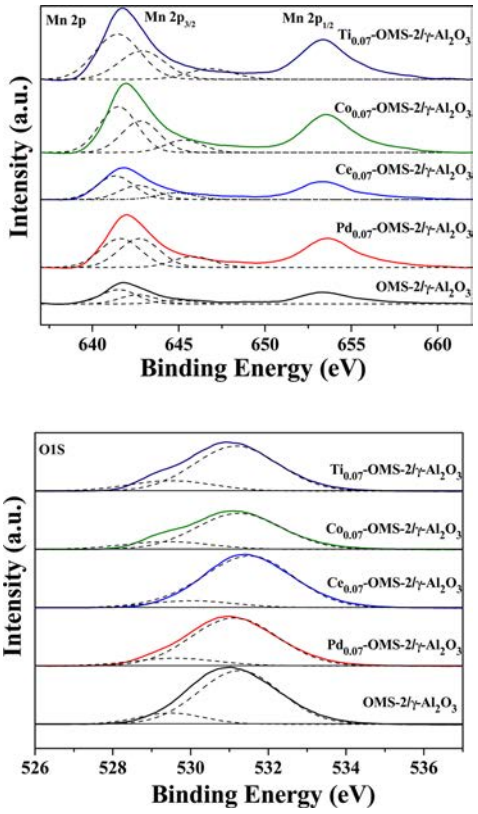

Figure 7. XPS spectra of metal-doped OMS-2/γ-Al_2O_3 catalysts.

attributed to the reduction of Mn_3O_4 to MnO.[44] $Pd_{0.07}$-OMS-2/γ-Al_2O_3 had a single sharp reduction peak at the low temperature of 70 °C due to the reduction of PdOx, indicating $Pd_{0.07}$-OMS-2/γ-Al_2O_3 had high redox ability and Pd was well dispersed, which was beneficial for *o*-xylene conversion, CO_2 selectivity, and CO_x yield. Further, for the $Ce_{0.07}$-OMS-2/γ-Al_2O_3 catalyst, a peak at the low temperature of 180 °C was observed, also suggesting its good oxidation ability.

The surface area, pore diameter, and pore volume of OMS-2/γ-Al_2O_3 catalysts were obtained on the basis of N_2 adsorption−desorption isotherms (Table 3). All catalysts had high surface areas above 200 m^2/g. Doping with metals increased the surface areas, which might be helpful for the improvement of catalytic activity of metal-doped catalysts. However, the rank order of surface area for the samples was not in agreement with that of catalytic activity, indicating that surface area was not the main factor determining the differences in catalytic activity for these metal-doped catalysts in *o*-xylene conversion. Both the pore diameter and pore volume decreased after metal doping, which also proved that part of the dopants entered into the OMS-2 structure and part were located in the OMS-2 framework or tunnels.[40]

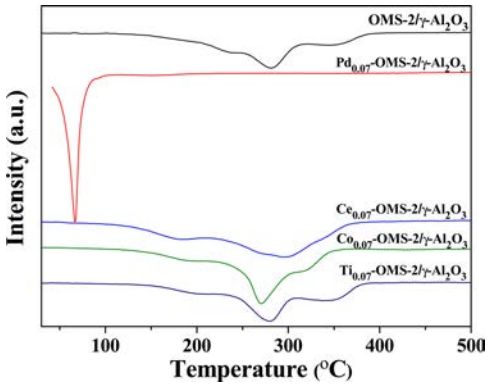

Figure 8. H_2-TPR profiles of metal-doped OMS-2/γ-Al_2O_3 catalysts.

Table 3. Physical Properties of the Metal-Doped OMS-2/γ-Al_2O_3 Catalysts

catalysts	surface area (m^2/g)	pore diameter (nm)	pore volume (cm^3/g)
OMS-2/γ-Al_2O_3	212.1	14.9	0.79
$Pd_{0.07}$-OMS-2/γ-Al_2O_3	234.2	9.8	0.57
$Ce_{0.07}$-OMS-2/γ-Al_2O_3	228.0	10.0	0.55
$Co_{0.07}$-OMS-2/γ-Al_2O_3	275.5	12.1	0.84
$Ti_{0.07}$-OMS-2/γ-Al_2O_3	248.8	9.8	0.61

3.3. Effect of Doping Site. XRD indicated that the all catalysts appeared to only contain OMS-2 and Al_2O_3 phases; therefore, the possibility of having a second metal phase could be ruled out. At the same time, ICP-OES results showed that both K^+ and Mn^{2+} concentrations decreased after doping with metals, while the K/Mn ratio clearly decreased with Ce doping and in contrast increased with Pd, Co, and Ti doping (Table 4).

Table 4. K^+ and Mn^{2+} Content Detection of the Metal-Doped OMS-2/γ-Al_2O_3 Catalysts by ICP-OES

catalysts	K^+ detected (mg/L)	Mn^{2+} (mg/L)	K/Mn detected (molar ratio)
OMS-2/γ-Al_2O_3	1.048	15.402	**0.096**
$Pd_{0.07}$-OMS-2/γ-Al_2O_3	0.96	14.308	**0.099**
$Ce_{0.07}$-OMS-2/γ-Al_2O_3	0.855	14.530	**0.083**
$Co_{0.07}$-OMS-2/γ-Al_2O_3	1.033	14.281	**0.102**
$Ti_{0.07}$-OMS-2/γ-Al_2O_3	0.981	14.122	**0.098**
$Ce_{0.07}$-OMS-2/γ-Al_2O_3 (ion exchange)	0.605	14.009	**0.043**

Table 2. XPS Results of the Metal-Doped OMS-2/γ-Al_2O_3 Catalysts

	BE (eV)			BE (eV)		
catalysts	Mn^{4+}	Mn^{3+}	$Mn^{3+}/(Mn^{3+}+Mn^{4+})$ (%)	O_{latt}	O_{sur}	$O_{sur}/(O_{latt}+O_{sur})$ (%)
OMS-2/γ-Al_2O_3	642.6	641.6	62.1	529.5	531.3	85.8
$Pd_{0.07}$-OMS-2/γ-Al_2O_3	642.7	641.7	50.0	529.5	531.4	**90.5**
$Ce_{0.07}$-OMS-2/γ-Al_2O_3	642.6	641.4	60.5	529.5	531.1	**88.0**
$Co_{0.07}$-OMS-2/γ-Al_2O_3	642.8	641.5	59.4	529.4	531.2	82.5
$Ti_{0.07}$-OMS-2/γ-Al_2O_3	642.9	641.5	61.3	529.5	531.2	81.4

DOI: 10.1021/acs.jpcc.6b00870
J. Phys. Chem. C 2016, 120, 6136−6144

These results proved that Ce ions might be mainly doped into the tunnel by substituting for K species, and Pd, Co, and Ti might be mainly doped into the framework by substituting for Mn species. During the nucleation and growth processes, metal ions could replace K in the VIII-fold tunnel sites to maintain the structural integrity, which should result in a loss of K^+. On the other hand, metal species can compete with Mn and fill a VI-fold site in the framework of OMS-2 in the preparation process. Metal doping into the OMS-2 structure in the octahedral framework and/or in the tunnels is generally governed by the crystal radii and the coordination of the dopant cations.[45] The crystal radii of VIII-fold coordinated Ce^{3+} (1.28 Å) and Ce^{4+} (1.11 Å) are more similar to that of VIII-fold coordinated K^+ (1.65 Å) than to those of low spin Mn^{3+} (0.72 Å), VI-fold coordinated high spin Mn^{3+} (0.785 Å), and VI-fold coordinated Mn^{4+} (0.67 Å). However, the crystal radii of VI-fold coordinated Pd^{2+} (1.0 Å), Pd^{4+} (0.755 Å), Co^{2+} (0.79 Å), Co^{3+} (0.685 Å), Ti^{4+}(0.745 Å), and Ti^{3+}(0.81 Å) are much smaller than that of K^+ (1.65 Å) but close to those of VI-fold coordinated low spin Mn^{3+} (0.72 Å), VI- fold coordinated high spin Mn^{3+} (0.785 Å), and VI-fold coordinated Mn^{4+} (0.67 Å). Therefore, it was highly possible that Ce existed in the tunnel sites rather than in the framework sites. On the contrary, Pd, Co, and Ti might mainly exist in the framework. Moreover, $Ce_{0.07}$-OMS-2/Al_2O_3 prepared by the ion-exchange method, which had lower K/Mn (Table 4), exhibited higher catalytic activity than that prepared by the hydrothermal method with high K/Mn (Figure 9). It could be deduced that doping metal into the tunnel by replacing K^+ might be helpful for the increase in catalytic activity of metal-doped OMS-2/Al_2O_3. The corresponding mechanism will be studied in detail in future work.

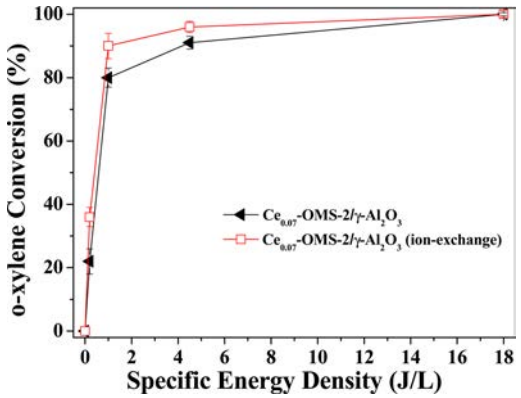

Figure 9. *o*-Xylene conversion using $Ce_{0.07}$-OMS-2/Al_2O_3 prepared by ion-exchange method and hydrothermal method.

3.4. Inhibiting Formation of Byproducts. To examine the ability of catalysts to inhibit byproduct formation, the outlet O_3 and NO_x concentrations were measured. Figure 10a gives the O_3 outlet concentrations before and after metal-doped OMS-2/γ-Al_2O_3 catalysts were introduced into the nonthermal plasma system. With the presence of catalysts, the O_3 outlet concentration was greatly decreased. When $Pd_{0.07}$-OMS-2/γ-Al_2O_3 and $Ce_{0.07}$-OMS-2/γ-Al_2O_3 catalysts were introduced, the O_3 outlet concentration was greatly reduced and near zero. Notably, the sequence of ability for inhibiting O_3 formation was in accordance with that of the catalytic activity of catalysts for *o*-xylene conversion. Ozone was catalytically decomposed and formed highly active reactive oxygen species.[26] These active oxygen species could efficiently oxidize *o*-xylene. Figure 10b shows the NO_x outlet concentration as a function of SED with and without metal-doped OMS-2 catalysts. Most of NO_x were NO_2 in our experiment because some active molecules and radicals such as O_3 and atomic oxygen produced in the discharge could oxidize NO to NO_2, which resulted in less NO production. It could be seen that the NO_x outlet concentration was reduced when catalysts were added. In particular, much lower amounts of NO_x were detected with addition of $Pd_{0.07}$-OMS-2/γ-Al_2O_3. The NO_x concentration was only 280 ppb with a SED of 18 J/L. These findings indicated that the OMS-2/γ-Al_2O_3 series of catalysts could efficiently reduce the production of byproducts.

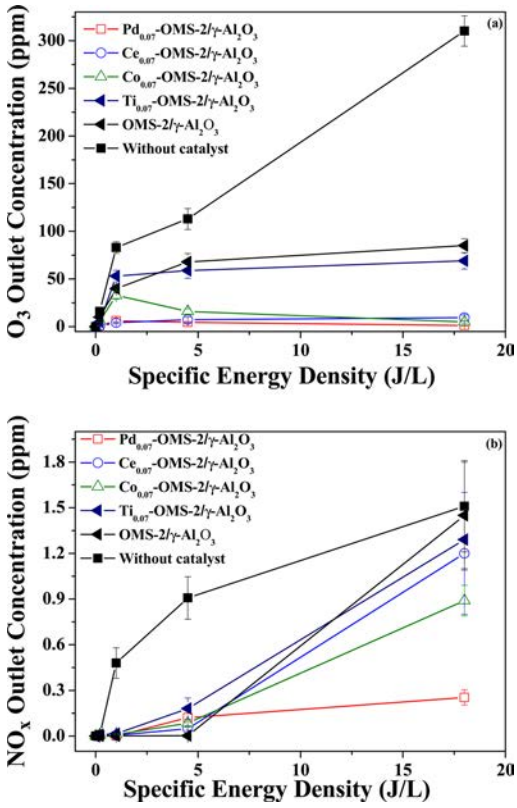

Figure 10. Byproducts of (a) O_3 and (b) NO_x with metal-doped OMS-2/γ-Al_2O_3 catalysts.

In order to determine the intermediate and final products of *o*-xylene oxidation in the plasma-catalytic processes, online FT-IR spectra were measured and shown in Figure 11. Products including CO_2, CO, CH_3CHO, $HCOOH/CH_3COOH$, and HNO_3 were observed and increased with the increase of SED. Peaks at 1122 and 1031 cm^{-1} could be assigned to C−O vibration modes.[46] Metal-doped OMS-2/γ-Al_2O_3 catalysts could oxidize *o*-xylene to CH_3CHO and/or CH_3COOH and further oxidize CH_3CHO and/or CH_3COOH to CO or CO_2.

4. CONCLUSIONS

In this study, metal-doped OMS-2/γ-Al_2O_3 catalysts placed downstream of the discharge zone were studied for removal of *o*-xylene in air. With the introduction of catalysts, *o*-xylene removal efficiency, CO_2 selectivity and CO_x yield could be significantly improved. The emission of undesirable byproducts such as O_3 and NO_x was also remarkably suppressed by metal-doped OMS-2/γ-Al_2O_3 catalysts. $Pd_{0.07}$-OMS-2/γ-Al_2O_3 and $Ce_{0.07}$-OMS-2/γ-Al_2O_3 had excellent catalytic activity for *o*-

DOI: 10.1021/acs.jpcc.6b00870
J. Phys. Chem. C 2016, 120, 6136−6144

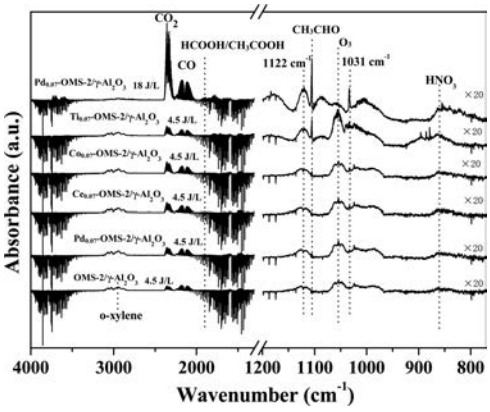

Figure 11. Online FT-IR spectra during the process of oxidizing *o*-xylene in air with OMS-2/γ-Al_2O_3 series of catalysts.

xylene removal including high *o*-xylene conversion, CO_2 selectivity, CO_x yield and byproducts suppression. Notably, $Pd_{0.07}$-OMS-2/γ-Al_2O_3 addition led to 100% *o*-xylene conversion, 80% CO_2 selectivity, and 95% CO_x yield at a low SED of 18 J/L. Both catalysts had abundant surface defects for absorbing and activating oxygen, more surface oxygen, and high redox activity. These factors all improved the catalytic activity toward oxidation of o-xylene. Furthermore, metal ions replacing K^+ in the tunnel sites could increase the catalytic activity, considering high catalytic activity and low K^+/Mn ratio of the $Ce_{0.07}$-OMS-2/γ-Al_2O_3 catalyst. The OMS-2/γ-Al_2O_3 series of catalysts could dissociate ozone, and produced active oxygen species that could oxidize *o*-xylene to CH_3CHO and/or CH_3COOH and further oxidize CH_3CHO and/or CH_3COOH to CO or CO_2.

AUTHOR INFORMATION

Corresponding Author

*Tel: +86 10 62849123. Fax: +86 10 62849121. E-mail: cbzhang@rcees.ac.cn.

Notes

The authors declare no competing financial interest.

ACKNOWLEDGMENTS

This work was financially supported by the National Natural Science Foundation of China (Nos. 51208497 and 21422706) and the National High Technology Research and Development Program of China (No. 2012AA062702).

REFERENCES

(1) Khan, F. I.; Ghoshal, A. K. Removal of Volatile Organic Compounds from Polluted Air. *J. Loss Prev. Process Ind.* **2000**, *13*, 527−545.
(2) Li, W. B.; Wang, J. X.; Gong, H. Catalytic Combustion of VOCs on Non-noble Metal Catalysts. *Catal. Today* **2009**, *148*, 81−87.
(3) Lee, H. M.; Chang, M. B. Abatement of Gas-phase p-xylene via Dielectric Barrier Discharges. *Plasma Chem. Plasma Process.* **2003**, *23*, 541−558.
(4) Ağıral, A.; Boyadjian, C.; Seshan, K.; Lefferts, L.; Gardeniers, J. G. E. Pathway Study on Dielectric Barrier Discharge Plasma Conversion of Hexane. *J. Phys. Chem. C* **2010**, *114*, 18903−18910.
(5) Demidyuk, V.; Christopher Whitehead, J. Influence of Temperature on Gas-phase Toluene Decomposition in Plasma-catalytic System. *Plasma Chem. Plasma Process.* **2007**, *27*, 85−94.
(6) Subrahmanyam, Ch.; Magureanu, M.; Laub, D.; Renken, A.; Kiwi-Minsker, L. Nonthermal Plasma Abatement of Trichloroethylene Enhanced by Photocatalysis. *J. Phys. Chem. C* **2007**, *111*, 4315−4318.
(7) Li, Y. Z.; Fan, Z. Y.; Shi, J. W.; Liu, Z. Y.; Shangguan, W. F. Post Plasma-catalysis for VOCs Degradation Over Different Phase Structure MnO_2 Catalysts. *Chem. Eng. J.* **2014**, *241*, 251−258.
(8) Wang, W. Z.; Wang, H. L.; Zhu, T. L.; Fan, X. Removal of Gas Phase Low-concentration Toluene over Mn, Ag and Ce Modified HZSM-5 Catalysts by Periodical Operation of Adsorption and Non-thermal Plasma Regeneration. *J. Hazard. Mater.* **2015**, *292*, 70−78.
(9) Lu, M. J.; Huang, R.; Wu, J. L.; Fu, M. L.; Chen, L. M.; Ye, D. Q. On the Performance and Mechanisms of Toluene Removal by FeO_x/SBA-15-assisted Non-thermal Plasma at Atmospheric Pressure and Room Temperature. *Catal. Today* **2015**, *242*, 259−265.
(10) Guo, Y. F.; Ye, D. Q.; Chen, K. F.; He, J. C.; Chen, W. L. Toluene Decomposition Using a Wire-plate Dielectric Barrier Discharge Reactor with Manganese Oxide Catalyst in situ. *J. Mol. Catal. A: Chem.* **2006**, *245*, 93−100.
(11) Zhu, T. L.; Wang, M. Y.; Li, X. M. Removal of Low-concentration BTX in Air Using a Combined Plasma Catalysis System. *Chemosphere* **2009**, *75*, 1301−1306.
(12) Subrahmanyam, Ch.; Renken, A.; Kiwi-Minsker, L. Catalytic Non-thermal Plasma Reactor for Abatement of Toluene. *Chem. Eng. J.* **2010**, *160*, 677−682.
(13) Ogata, A.; Yamanouchi, K.; Mizuno, K.; Kushiyama, S.; Yamamoto, T. Decomposition of Benzene Using Alumina-hybrid Plasma Reactors. *IEEE Trans. Ind. Appl.* **1999**, *35*, 1289−1295.
(14) Ogata, A.; Einaga, H.; Kabashima, H.; Futamura, S.; Kushiyama, S.; Kim, H. H. Effective Combination of Nonthermal Plasma and Catalysts for Decomposition of Benzene in Air. *Appl. Catal., B* **2003**, *46*, 87−95.
(15) Kim, H. H.; Oh, S. M.; Ogata, A.; Futamura, S. Decomposition of Gas-phase Benzene Using Plasma-driven Catalyst (PDC) Reactor Packed with Ag/TiO_2 Catalyst. *Appl. Catal., B* **2005**, *56*, 213−220.
(16) Li, J.; Han, S. T.; Bai, S. P.; Shi, X. C.; Han, S. L.; Song, H.; Pu, Y. K.; Zhu, X. M.; Chen, W. C. Effect of Pt/γ-Al_2O_3 Catalyst on Nonthermal Plasma Decomposition of Benzene and Byproducts. *Environ. Eng. Sci.* **2011**, *28*, 395−403.
(17) Roland, U.; Holzer, F.; Kopinke, F. D. Combination of Non-thermal Plasma and Heterogeneous Catalysis for Oxidation of Volatile Organic Compounds. Part 2. Ozone Decomposition and Deactivation of γ-Al_2O_3. *Appl. Catal., B* **2005**, *58*, 217−226.
(18) Harling, A. M.; Glover, D. J.; Whitehead, J. C.; Zhang, K. The Role of Ozone in the Plasma-catalytic Destruction of Environmental Pollutants. *Appl. Catal., B* **2009**, *90*, 157−161.
(19) Dhandapani, B.; Oyama, S. T. Gas Phase Ozone Decomposition Catalysts. *Appl. Catal., B* **1997**, *11*, 129−166.
(20) Wang, C. X.; Ma, J. Z.; Liu, F. D.; He, H.; Zhang, R. D. The Effects of Mn^{2+} Precursors on the Structure and Ozone Decomposition Activity of Cryptomelane-Type Manganese Oxide (OMS-2) Catalysts. *J. Phys. Chem. C* **2015**, *119*, 23119−23126.
(21) Sun, H.; Chen, S.; Wang, P.; Quan, X. Catalytic Oxidation of Toluene over Manganese Oxide Octahedral Molecular Sieves (OMS-2) Synthesized by Different Methods. *Chem. Eng. J.* **2011**, *178*, 191−196.
(22) Sanz, O.; Delgado, J. J.; Navarro, P.; Arzamendi, G.; Gandía, L. M.; Montes, M. VOCs Combustion Catalysed by Platinum Supported on Manganese Octahedral Molecular Sieves. *Appl. Catal., B* **2011**, *110*, 231−237.
(23) Tian, H.; He, J. H.; Zhang, X. D.; Zhou, L.; Wang, D. H. Facile Synthesis of Porous Manganese Oxide K-OMS-2 Materials and Their Catalytic Activity for Formaldehyde Oxidation. *Microporous Mesoporous Mater.* **2011**, *138*, 118−122.
(24) Li, D. Y.; Liu, H. D.; Chen, Y. F. Synthesis of Manganese Oxide Octahedral Sieve and Their Application in Catalytic Oxidation of Benzene. *Chin. J. Environ. Sci.* **2011**, *32*, 3657−3661.
(25) Genuino, H. C.; Dharmarathna, S.; Njagi, E. C.; Mei, M. C.; Suib, S. L. Gas-phase Total Oxidation of Benzene, Toluene, Ethylbenzene, and Xylenes Using Shape-selective Manganese Oxide

DOI: 10.1021/acs.jpcc.6b00870
J. Phys. Chem. C 2016, 120, 6136−6144

and Copper Manganese Oxide Catalysts. *J. Phys. Chem. C* **2012**, *116*, 12066−12078.
(26) Ousmane, M.; Perrussel, G.; Yan, Z.; Clacens, J. M.; De Campo, F.; Pera-Titus, M. Highly Selective Direct Amination of Primary Alcohols over a Pd/K-OMS-2 Catalyst. *J. Catal.* **2014**, *309*, 439−452.
(27) Chen, X.; Shen, Y. F.; Suib, S. L.; O'Young, C. L. Characterization of Manganese Oxide Octahedral Molecular Sieve (M-OMS-2) Materials with Different Metal Cation Dopants. *Chem. Mater.* **2002**, *14*, 940−948.
(28) Polverejan, M.; Villegas, J. C.; Suib, S. L. Higher Valency Ion Substitution Into the Manganese Oxide Framework. *J. Am. Chem. Soc.* **2004**, *126*, 7774−7775.
(29) Li, Y. Z.; Fan, Z. Y.; Shi, J. W.; Liu, Z. Y.; Zhou, J. W.; Shuangguan, W. F. Removal of Volatile Organic Compounds (VOCs) at Room Temperature Using Dielectric Barrier Discharge and Plasma-Catalysis. *Plasma Chem. Plasma Process.* **2014**, *34*, 801−810.
(30) Wang, Y. F.; Zhang, C. B.; Liu, F. D.; He, H. Well-dispersed Palladium Supported on Ordered Mesoporous Co_3O_4 for Catalytic Oxidation of o-xylene. *Appl. Catal., B* **2013**, *142−143*, 72−79.
(31) Einaga, H.; Maeda, N.; Teraoka, Y. Effect of Catalyst Composition and Preparation Conditions on Catalytic Properties of Unsupported Manganese Oxides for Benzene Oxidation with Ozone. *Appl. Catal., B* **2013**, *142−143*, 406−413.
(32) Ye, L. L.; Feng, F. D.; Liu, J.; Liu, Z.; Yan, K. P. Plasma Induced Toluene Decomposition on Alumina-supported Mn-based Composite Oxides Catalysts. *J. Phys.: Conf. Ser.* **2013**, *418*, 012116.
(33) Subrahmanyam, Ch.; Mangureanu, M.; Laub, D.; Renken, A.; Kiwi-Minsker, L. Nonthermal Plasma Abatement of Trichloroethylene Enhanced by Photocatalysis. *J. Phys. Chem. C* **2007**, *111*, 4315−4318.
(34) Luo, J.; Zhang, Q.; Huang, A.; Suib, S. L. Total Oxidation of Volatile Organic Compounds with Hydrophobic Cryptomelane-type Octahedral Molecular Sieves. *Microporous Mesoporous Mater.* **2000**, *35−36*, 209−217.
(35) Liu, J.; Makwana, V.; Cai, J.; Suib, S. L.; Aindow, M. Effect of Alkali Metal and Ammonium Cation Templates on Nanofibrous Cryptomelane-type Manganese Oxide Octahedral Molecular Sieves (OMS-2). *J. Phys. Chem. B* **2003**, *107*, 9185−9194.
(36) Cook, J. W.; Sayers, D. E. Criteria for Automatic X-ray Absorption Fine Structure Background Removal. *J. Appl. Phys.* **1981**, *52*, 5024−5031.
(37) Ankudinov, A. L.; Ravel, B.; Rehr, J. J.; Conradson, S. D. Real-space Multiple-scattering Calculation and Interpretation of X-ray-absorption Near-edge Structure. *Phys. Rev. B: Condens. Matter Mater. Phys.* **1998**, *58*, 7565−7576.
(38) Wang, R. C.; Su, W. S. Valence Control Periodic Structures in Cu-doped ZnO Nanowires. *J. Alloys Compd.* **2016**, *654*, 1−7.
(39) Khan, H.; Berk, D. Selenium Modified Oxalate Chelated Titania: Characterization, Mechanistic and Photocatalytic Studies. *Appl. Catal., A* **2015**, *505*, 285−301.
(40) Kingondu, C. K.; Opembe, N.; Chen, C. H.; Ngala, K.; Huang, H.; Lyer, A.; Garces, H. F.; Suib, S. L. Manganese Oxide Octahedral Molecular Sieves (OMS-2) Multiple Framework Substitutions: A New Route to OMS-2 Particle Size and Morphology Control. *Adv. Funct. Mater.* **2011**, *21*, 312−323.
(41) Liu, F. D.; Shan, W. P.; Lian, Z. H.; Xie, L. J.; Yang, W. W.; He, H. Novel MnWOx Catalyst with Remarkable Performance for Low Temperature NH_3-SCR of NOx. *Catal. Sci. Technol.* **2013**, *3*, 2699−2707.
(42) Wu, Y. S.; Lu, Y.; Song, C. J.; Ma, Z. C.; Xing, S. T.; Gao, Y. Z. A Novel Redox-precipitation Method for the Preparation of α-MnO_2 with a High Surface Mn^{4+} Concentration and its Activity Toward Complete Catalytic Oxidation of o-xylene. *Catal. Today* **2013**, *201*, 32−39.
(43) Tang, X. F.; Li, Y. G.; Huang, X. M.; Xu, Y. D.; Zhu, H. Q.; Wang, J. G.; Shen, W. J. MnO_x-CeO_2 Mixed Oxide Catalysts for Complete Oxidation of Formaldehyde: Effect of Preparation Method and Calcination Temperature. *Appl. Catal., B* **2006**, *62*, 265−273.
(44) Kapteljn, F.; Smgoredjo, L.; Andreml, A.; Moulijn, J. A. Activity and Selectivity of Pure Manganese Oxides in the Selective Catalytic Reduction of Nitric Oxide with Ammonia. *Appl. Catal., B* **1994**, *3*, 173−189.
(45) Shannon, R. D. Revised Effective Ionic Radii and Systematic Studies of Interatomic Distances in Halides and Chalcogenides. *Acta Crystallogr., Sect. A: Cryst. Phys., Diffr., Theor. Gen. Crystallogr.* **1976**, *32*, 751−767.
(46) Kersszegi, C.; Ferri, D.; Mallat, T.; Baiker, A. Unraveling the Surface Reactions During Liquid-phase Oxidation of Benzyl Alcohol on Pd/Al_2O_3: An in Situ ATR-IR Study. *J. Phys. Chem. B* **2005**, *109*, 958−967.

DOI: 10.1021/acs.jpcc.6b00870
J. Phys. Chem. C 2016, 120, 6136−6144